Date of publication xxxx 00, 0000, date of current version Jan 10, 2022.

Digital Object Identifier 10.1109/TQE.2020.DOI

Discriminating Quantum States in the Presence of a Deutschian CTC: a Simulation Analysis

LEONARDO BACCIOTTINI[1†], LUCIANO LENZINI[2], ENZO MINGOZZI[3] AND GIUSEPPE ANASTASI[4].

[1]University of Florence, Florence, 50121 ITALY (email: baccio.leonardo@gmail.com)
[†]Dipartimento di Ingegneria dell'Informazione, University of Pisa, Pisa, 56126 ITALY
[2]Dipartimento di Ingegneria dell'Informazione, University of Pisa, Pisa, 56126 ITALY (email: l.lenzini@iet.unipi.it)
[3]Dipartimento di Ingegneria dell'Informazione, University of Pisa, Pisa, 56126 ITALY (email: enzo.mingozzi@unipi.it)
[4]Dipartimento di Ingegneria dell'Informazione, University of Pisa, Pisa, 56126 ITALY (email: giuseppe.anastasi@unipi.it)

Corresponding author: Leonardo Bacciottini (email: baccio.leonardo@gmail.com).

ABSTRACT In a paper published in 2009, Brun *et al.* proved that in the presence of a D-CTC one can map K distinct non-orthogonal states (hereafter input set) to the standard orthonormal basis of a K-dimensional state space. To implement this result, the authors propose a quantum circuit which includes, among SWAP gates, a fixed set of controlled operators (boxes) and an algorithm for determining the unitary transformations carried out by such boxes. To our knowledge, what is still missing to complete the picture is an analysis evaluating the performance of the above circuit from an engineering perspective. The objective of this paper is therefore to address this gap throughout an in-depth simulation analysis which exploits the approach proposed by Brun *et al.* in 2017. This approach relies on multiple copies of an input state, multiple iterations of the circuit until a fixed point is (almost) reached. The performance analysis led us to a number of findings. First, the number of iterations is significantly high even if the number of states to be discriminated against is small, such as 2 or 3. Second, we envision that such a number may be shortened as there is plenty of room to improve the unitary trasformation acting in the aforementioned controlled boxes. Third, we also revealed a relationship between the number of iterations required to get close to the fixed point and the Chernoff limit of the input set used: the higher the Chernoff bound the smaller the number of iterations. A comparison, although partial, with another quantum circuit discriminating the non-orthogonal states, proposed by Nareddula *et al.* in 2018, is carried out and differences are highlighted.

INDEX TERMS Classical simulation of quantum systems, Benchmarking and performance characterization.

I. INTRODUCTION AND STATE OF THE ART

Closed timelike curves (hereafter, CTCs) have been debated for some time now. Since Deutsch's seminal work [1], quantum information theorists have become involved in the discussion.

Although there are now several models of CTCs under active consideration by the quantum information community, we focus on the most prominent one for describing quantum systems in the presence of CTCs, introduced by Deutsch [1]. Refer to [2] and the references in it for information on other models.

Several researchers have argued that, for example, "Deutschian" closed timelike curves (D-CTCs) can help solve NP-complete problems [3], that a D-CTC-assisted classical or quantum computer has computational power equivalent to that of PSPACE [4], that a a D-CTC would be able to violate the Heisenberg's uncertainty principle [5], and that a D-CTC-assisted quantum computer can perfectly distinguish an arbitrary set of non-orthogonal states [6]. This paper focuses on the last issue. The choice of this focus was, to some degree, motivated by the fact that quantum discrimination underpins various applications in quantum information processing tasks. Readers interested in exploring this research pathway may wish to consult [7].

Treatments of CTCs in the quantum information literature generally distinguish two subsystems: the chronology-

violating system, which passes through the CTC and returns to its own past, and the chronology-respecting system, which does not itself pass through the CTC but can interact with the chronology-violating subsystem.

In a paper published in 2009, Brun *et al.* [6] proved that in the presence of a D-CTCs one can map K distinct non-orthogonal states to the standard orthonormal basis of a K-dimensional state space. Moreover, the paper conveys: 1) the basic architecture of a quantum circuit to discriminate non-orthogonal states, in terms of controlled boxes (acting solely on closed timelike curves) other than SWAP gates, and 2) an algorithm for deriving unitary transformations carried out by such boxes.

To our knowledge, what is still missing to complete the picture is a deep analysis evaluating the performance of the quantum circuit shown in [6] from an engineering perspective. The purpose of this paper is therefore to address this gap by exploiting the simulation approach for D-CTC described in [2]. The major advantage of this approach is that it has a guaranteed fixed-point convergence, which is exactly what we seek. On the other hand, the main drawbacks are: 1) it could take a long time to converge to a fixed point, whose computation is known to be a PSPACE-complete problem [4]; 2) it requires, in general, many copies of the initial input state.

Thus, our assessment boils down to evaluating the behavior of the *convergence speed towards a fixed point* when the quantum circuit is fed by input sets of states with very different characteristics. This type of performance analysis gave us an invaluable insight into the impact on the convergence rate of the level of overlapping between the states belonging to their input sets. A comparison of performance, albeit partial, with the quantum circuit for discriminating non-orthogonal states, published by Nareddula *et al.* [8] is provided and findings are highlighted. This paper builds upon the research work undertaken in the M.SC. thesis by Bacciottini [9].

The rest of the paper proceeds as follows. The following section provides a basic background of the closed timelike curves (CTCs) whereas Section III sketches the quantum circuits from [6] and [8]. Section IV defines the simulative approach used to evaluate the performances of both models and the metric for such evaluation. Section V deals with the software architecture we developed and the equipment we used, whereas Section VI describes the assessment of both models. Section VII outlines the impact of the various input sets defined in the paper to the number of iterations to land on the fixed point. Conclusions and perspectives are discussed in Section VIII.

II. CLOSED TIMELIKE CURVES BACKGROUND

Before evaluating and comparing either model, we mainly outline a few concepts related to quantum operations formalism [10] which provides the tools to describe the evolution of the Deutschian model of CTC (below, D-CTC).

D-CTCs are formally specified by means of the following objects:

- the initial density operator $\rho_{CR} = |\psi\rangle\langle\psi|$ for the chronology-respecting system (hereafter, CR), where $|\psi\rangle$ is a pure input state for the CR, and
- the interaction unitary U between CR and the chronology-violating system (hereafter, CTC).

The model in [1] assumes that CR and CTC are not interacting until the CTC emerges from the past mouth of its wormhole, i.e. the initial state of CR and CTC starts in a tensor state $\rho_{CR} \otimes \rho_{CTC}$, where ρ_{CTC} is a density operator for the CTC state. Systems CR and CTC interact according to a unitary U, leading to the following state after the interaction

$$\rho_{CR}\otimes\rho_{CTC} \rightarrow U(\rho_{CR}\otimes\rho_{CTC})U^\dagger = U(|\psi\rangle\langle\psi|\otimes\rho_{CTC})U^\dagger \tag{1}$$

Note: Even though (1) is formulated in terms of a pure input state $|\psi\rangle$ it can be directly generalized to mixed inputs as shown in [11].

The reduced density matrix ρ'_{CR} of the chronology-respecting system CR after the interaction is

$$\rho'_{CR} = Tr_{CTC}\{U(|\psi\rangle\langle\psi| \otimes \rho_{CTC})U^\dagger\}. \tag{2}$$

On the other hand, D-CTCs impose a self-consistency condition, in which the density operator ρ_{CTC} of the CTC is the same, both before and after it enters the wormhole. Formally,

$$\rho_{CTC} = \mathcal{N}_{U,\rho}(\rho_{CTC}) = Tr_{CR}\{U(|\psi\rangle\langle\psi| \otimes \rho_{CTC})U^\dagger\}. \tag{3}$$

Mathematically, this can be seen as Nature finding a fixed-point solution of the channel $\mathcal{N}_{U,\rho}$ that depends on the chronology respecting system CR [1].

The output state ρ'_{CR} is in general a nonlinear function of the input state $|\psi\rangle$, because ρ'_{CR} (2) depends on both $|\psi\rangle$ and ρ_{CTC}, and ρ_{CTC} (3), in turn, depends on $|\psi\rangle$. This lack of linearity allows the limits of quantum mechanics to be overcome. Specifically, as pointed out in [6], a party having access to a CTC (hereafter called CTC-assisted party) could perfectly distinguish any set of non-orthogonal quantum states which consequently implies the violation of the Holevo bound [12]. In the next section we outline the work by Brun *et al.* [6], which implements one of the two recipes assessed in the paper.

For ease of writing, when referring to the circuits and algorithms described in [6] and [8], we use the acronyms BHW and NBP respectively, from the initials of authors' surnames. Furthermore, the expressions BHW/NBP quantum circuit and BHW/NBP model are used interchangeably.

III. QUANTUM CIRCUITS DESCRIPTION

This section outlines the quantum circuits that will be evaluated and compared to each other. It also provides an overview of the simulative approach used to evaluate the performance of both quantum circuits.

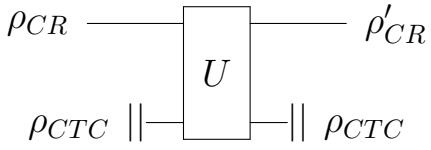

FIGURE 1: A quantum circuit showing a D-CTC in an interaction U. The CTC state is the same at the beginning and at the end of the interaction, and this is expressed by the *wormhole* symbols "||".

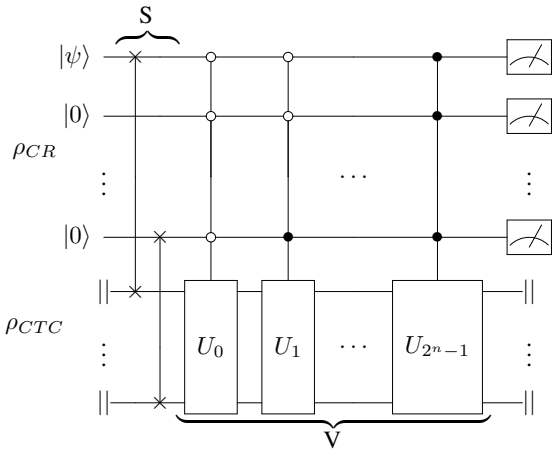

FIGURE 2: BHW quantum circuit.

A. BHW QUANTUM CIRCUIT

Brun *et al.* [6] proved that, given a set $\{|\psi_k\rangle\}_{k=0}^{K-1}$ of distinct non-orthogonal states in a space of dimension $K = 2^n$, then a party with access to an K-dimensional D-CTC can implement the following map

$$|\psi_k\rangle \rightarrow |k\rangle \, \forall k \in \{0, 1, 2, \ldots, K-1\} \tag{4}$$

where states $|k\rangle$ are a standard orthonormal basis (often called Computation Basis States or CBS for short) for the K-dimensional space. The quantum circuit that can perform this map is illustrated in Fig. 2, which is a generalization to any n of the circuit illustrated in [6] relative to case $n = 2$.

The CR and CTC registers contain n qubits each. The first qubit in the CR register is any qubit taken out from an input set $\{|\psi_k\rangle\}_{k=0}^{K-1}$, and the remaining $n-1$ qubits (ancillary qubits) are initialized to state $|0\rangle$. As shown in Fig. 2, the complete interaction unitary U - recall (1), (3) - is given by $U = VS$, where

$$S = SWAP(CR \leftrightarrow CTC) \tag{5}$$

and V is a controlled unitary from the CR to the CTC expressed as

$$V = \sum_{k=0}^{K-1} |k\rangle \langle k| \, U_k \tag{6}$$

The $\{U_k\}_{k=0}^{K-1}$ in (6) are a set of K unitary transformations acting just on the CTC system (see the boxes in Fig. 2) and are chosen in such a way that

$$U_k \, |\psi_k\rangle = |k\rangle \, \forall k \in \{0, 1, 2, \ldots, K-1\}. \tag{7}$$

To verify that the circuit of Fig. 2 implements the mapping in (4) let's take $\rho_{CR} = |\psi_k\rangle \langle\psi_k|$ as the input state of the CR. Before the interaction, the CTC is in the state ρ_{CTC} which must satisfy the self-consistency condition (3) for $|\psi\rangle = |\psi_k\rangle$. It is very simple to check that the solution $\rho_{CTC} = |k\rangle \langle k|$ satisfies the self-consistency condition and gives the desired output state (2), i.e. $|k\rangle$.

To guarantee the uniqueness of the solution of the self-consistency condition (3), a set of sufficient (but by no means necessary) constraints must hold, i.e.

$$\langle j| \, U_k \, |\psi_j\rangle \neq 0 \;\; \forall j \;\; and \;\; \forall k. \tag{8}$$

In addition to the aforementioned theorem, Brun *et al.* [6] provide an algorithm for the construction of the unitary transformations $\{U_k\}_{k=0}^{K-1}$ acting only on the CTC system, satisfying (8). The algorithm is outlined below using the pseudo-code shown in Fig. 3.

The set $\mathcal{S}$ (see Fig. 3) of non-orthogonal states $\{|\psi_k\rangle\}_{k=0}^{K-1}$ to be discriminated is given as input to the CR system (#1).

At the k^{th} iteration, the loop in Fig. 3 returns the matrix U_k. In order to achieve this, we must construct two different orthonormal bases $|b_m\rangle$ and $|c_m\rangle$, for $m = \{1, 2, \ldots, K\}$, that we will store in the empty sets $\mathcal{B}$ and $\mathcal{C}$ (#5, #6, #7) respectively.

The first element $|b_1\rangle$ in $\mathcal{B}$ is the $(k+1)^{th}$ element inside $\mathcal{S}$, which corresponds to $|\psi_k\rangle \otimes |0\rangle^{\otimes n-1}$ (#8).

The second element $|b_2\rangle$ in $\mathcal{B}$ is obtained by performing the *Gram-Schmidt* orthogonalization between $|b_1\rangle$ and any other state inside $\mathcal{S}$. For simplicity, we take the immediately subsequent state (#9).

The first element $|c_1\rangle$ in $\mathcal{C}$ is simply the CBS state $|k\rangle$ (#11). The second element $|c_2\rangle$ in $\mathcal{C}$ is obtained as a uniform superposition of all the other CBS states (#12).

There are only two linearly independent states in the set $\mathcal{S}$. For this reason, we complete $\mathcal{B}$ and $\mathcal{C}$ bases with any set of orthonormal states (#14). The freedom in the choice of these additional states has no impact on the performance of the algorithm. We will come back to this point later in Section VI-A3.

We use $\mathcal{B}$ and $\mathcal{C}$ elements to build the matrix U_k following the expression in (#15).

The loop is repeated for each possible value of k in $\{0, 1, \ldots, 2^n - 1\}$.

B. NBP QUANTUM CIRCUIT

The NBP quantum circuit shown in Fig. 4 was proposed by Nareddula *et al.* [8] for storing and retrieving n-bit classical information faithfully in the presence of a D-CTC in violation of the Holevo bound. It should be noted that the problems of encoding and decoding a string of classical bits in a qubit are equivalent to the problem of discrimination of non-orthogonal states [13].

1: $\mathcal{S}$ is the set of non-orthogonal, n-qubit state vectors $|\psi_k\rangle |0\rangle^{\otimes n-1}$ for $k \in 0 \dots 2^n - 1$, where $|\psi_k\rangle \equiv \cos \frac{\pi k}{2^n} |0\rangle + \sin \frac{\pi k}{2^n} |1\rangle$, sorted by ascending k.
2: $\mathcal{U}$ is the set which will contain all U_k matrices, for k $\in$ $0 \dots 2^n - 1$.
3: $\mathcal{U} \leftarrow \emptyset$
4: **for** k in $0 \dots 2^n - 1$ **do**
5: $\quad \mathcal{B}$ is the set which will contain the $\{|b_1\rangle, \dots, |b_n\rangle\}$ basis.
6: $\quad \mathcal{C}$ is the set which will contain the $\{|c_1\rangle, \dots, |c_n\rangle\}$ basis.
7: $\quad \mathcal{B} \leftarrow \emptyset, \mathcal{C} \leftarrow \emptyset$
8: $\quad |b_1\rangle \leftarrow \mathcal{S}[k]$
9: $\quad |b_2\rangle \leftarrow$ *gram_schmidt*$(\mathcal{S}[k+1 \mod 2^n], \mathcal{S}[k])$
10: $\quad \mathcal{B} \leftarrow \mathcal{B} \cup \{|b_1\rangle, |b_2\rangle\}$
11: $\quad |c_1\rangle \leftarrow |k\rangle$
12: $\quad |c_2\rangle \leftarrow \frac{\sum_{i \neq k} |i\rangle}{\sqrt{2^n - 1}}$
13: $\quad \mathcal{C} \leftarrow \mathcal{C} \cup \{|c_1\rangle, |c_2\rangle\}$
14: $\quad$ Fill $\mathcal{B}$ and $\mathcal{C}$ with any $n-2$ orthonormal state vectors.
15: $\quad U_k \leftarrow \sum_i |c_i\rangle \langle b_i|$, where $|b_i\rangle \in \mathcal{B}$ and $|c_i\rangle \in \mathcal{C}$
16: $\quad \mathcal{U} \leftarrow \mathcal{U} \cup U_k$
17: **end for**
18: Return $\mathcal{U}$

FIGURE 3: Pseudocode for BHW recipe implementation

Let k be the integer value representing an n-bit string $a_{n-1}, \dots, a_0$; k can obviously assume values in the interval $[0, 2^n - 1]$. Nareddula *et al.* map the possible values of k to a set $\{|\psi_k\rangle\}_{k=0}^{2^n-1}$ of $K = 2^n$ distinct non-orthogonal quantum states according to the map

$$k \rightarrow |\psi_k\rangle = \cos \frac{\pi k}{2^n} |0\rangle + \sin \frac{\pi k}{2^n} |1\rangle \quad \forall k \in \{0, 1, \dots, K-1\}. \tag{9}$$

It can be easily verified that the above states are evenly spaced pure states lying on the XZ-plane of the Bloch sphere. For reasons which will be explained in Section VII, this set will be called the $XZ(n)$-input set. Note that for $n = 2$, by varying k in the set $\{0, 1, 2, 3\}$, we reproduce the BB84 states $\{|0\rangle, |+\rangle, |1\rangle, |-\rangle\}$.

For retrieving the encoded information, Nareddula *et al.* employ the CTC-assisted circuit shown in Fig. 4 which maps each state $|\psi_k\rangle$ to the CBS state $|k\rangle$. The first qubit $|\psi\rangle$ of the Chronology Respecting system CR is the encoded qubit, whereas the others, all set to $|0\rangle$, are $n-1$ ancillary qubits. The unitary interaction of the circuit can be written as $U = CWTRS$, where C, W, T, R, and S are groups of gates highlighted in Fig. 4. Since it is used in the next section, we also define the unitary V as

$$V = CWTR. \tag{10}$$

To show the algorithm correctness, Nareddula *et al.* first prove that CTC input state $\rho_{CTC} = |k\rangle \langle k|$ is a fixed point of the Deutsch equation (Equation 3) if $|\psi\rangle = |\psi_k\rangle$, where $|k\rangle = |a_{n-1}, \dots, a_0\rangle$. In this case we can assume that CR input state is $|\psi\rangle \otimes |0\rangle^{\otimes n-1}$ and CTC state right out of the wormhole is $|k\rangle \langle k|$. Gate S simply swaps the states of the two systems, so that state $|\psi_k\rangle$ is now the state of the first CTC qubit. Then, gate R applies consecutive controlled rotations that transform the state $|\psi_k\rangle$ to $|0\rangle$. Hence, the CTC state is now $|0\rangle^{\otimes n}$, and gates T and W do not have any influence on it. Gate C performs the following action on the whole system (labels are added for clarity):

$$|k\rangle_{CR} \otimes |0\rangle_{CTC} \rightarrow |k\rangle_{CR} \otimes |0 \oplus k\rangle_{CTC} = |k\rangle_{CR} \otimes |k\rangle_{CTC}. \tag{11}$$

Measuring the CR system along the CBS enables the retrieval of the initially encoded n-bit string in $|\psi\rangle$ with a probability equal to one. Also note that the final state of the CTC is the same as the initial one entering the system, thus proving the self-consistency condition 3.

Finally, Nareddula *et al.* in [8] successfully demonstrate the uniqueness of the solution by exploiting the set of sufficient conditions provided by Brun *et al.* in [6]. We don't prove that here because these are fairly long algebraic calculations that are beyond the scope of this work. The interested reader can find the proof in [8].

Note on Complexity - Lastly, it must be pointed out that the NBP model has a quantum cost in the order of $O(n)$ with respect to the number n of classical bits encoded. The quantum cost of a circuit is expressed in terms of the number of primitive gates required to build it [14]. Instead, the BHW model has a cost in the order of at least $O(2^n)$, because it is composed of 2^n controlled unitaries $\{U_k\}_{k=0}^{K-1}$, which must also be decomposed in an equivalent combination of primitive quantum gates. This will definitely lead to an increase in the quantum cost.

IV. SIMULATIVE APPROACH OF A D-CTC, METRIC AND SCENARIOS

The iterative approach we used to simulate the presence of a D-CTC follows the scheme proposed in [11] and is shown by Fig. 5, where $|c\rangle$ is any initial pure state for the CTC system. $|\Psi_k\rangle \equiv |\psi_k\rangle |0\rangle^{\otimes n-1}$ are independent copies of the CR system and the unitary V is defined above for both BHW (6) and NBP (10) quantum circuits respectively. This approach is justified by the fact that consecutive applications of the quantum channel $\mathcal{N}_{U,\rho}(\rho_{CTC}) = \mathrm{Tr}_{CR}\{U(\rho_{CR} \otimes \rho_{CTC})U^\dagger\}$ make the CTC system state converge to the fixed point $|k\rangle \langle k|$ of the interaction. Formally,

$$\lim_{N \to \infty} \mathcal{N}_{U,\rho}^N(|c\rangle \langle c|) = |k\rangle \langle k|. \tag{12}$$

The interested reader can find the proof of (12) in [11].

From (12) it is clear that convergence towards the fixed point is asymptotic. From an engineering perspective, we're looking at the estimation of the metric $N_{land}(95\%)$, defined as follows:

$$N_{land}(95\%) = \min_N \{N : p(k, N) \geq 0.95\} \quad where \;\; p(k, N) = \mathrm{Tr}\{|k\rangle \langle k| \mathcal{N}_{U,\rho}^N(|c\rangle \langle c|)\} \tag{13}$$

For instance, if $N_{land}(95\%) = 15$ when the CR system is fed with $|\psi_5\rangle$, it means that after 15 iterations the output (Fig. 5) lands on state $|5\rangle \langle 5|$ with probability $p(5, 15) \geq 0.95$. We chose $N_{land}(95\%)$ because it is neatly visible in the

This article has been accepted for publication in a future issue of this journal, but has not been fully edited. Content may change prior to final publication. Citation information: DOI 10.1109/TQE.2022.3142531, IEEE Transactions on Quantum Engineering

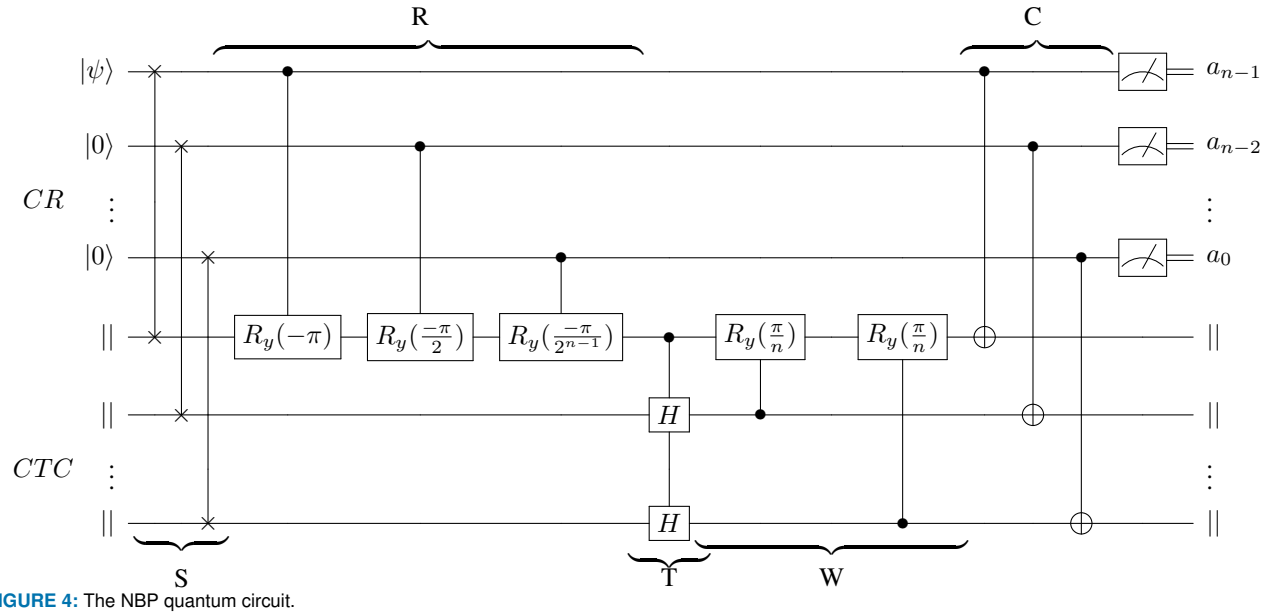

FIGURE 4: The NBP quantum circuit.

performance figures reported in Section VI, but we could have an $N_{land}(99\%)$ or something else.

As explained in [2], each iteration of a D-CTC simulation circuit requires an independent copy of the state $|\psi_k\rangle$, whatever k. Clearly, the smaller the value of $N_{land}(95\%)$, the better the performance of the algorithm. To evaluate the impact on $N_{land}(95\%)$ of

1) the value of n, i.e. the number of qubits of the CR and CTC systems,
2) the initial state $|c\rangle$ for the CTC system,
3) the state $|\psi_k\rangle$ of the CR system,

we define many scenarios, each identified by a specific triplet $(n, |c\rangle, |k\rangle)$. We performed an exhaustive performance evaluation on all possible $|c\rangle$ and $|k\rangle$ values (hereafter called parameters) for scenarios with $n = 2, 3, 4$.

The performance assessment in the paper draws on two metrics: $N_{land}(95\%)$ we just defined, whereas QCB (Quantum Chernoff Bound) pertains to the characterization of the input set. QCB will be introduced in Section VII where it is first used.

The implementation of the above simulative approach on a quantum computer requires a major problem to be addressed: the number of qubits required by the simulative environment (Fig. 5) increases linearly with the number of iterations N. This makes practically impossible to reach $N_{land}(95\%)$ using quantum simulators like *Qiskit Aer QasmSimulator* [15], which supports up to 30 qubits. We found a way to fix this problem which may be useful to anyone facing the same situation. For this reason, we detail our solution in Appendix B .

V. SOFTWARE ARCHITECTURE AND EQUIPMENT

As we said previously, scenarios were simulated by using *Qiskit Aer QasmSimulator* [15] as backend (unless otherwise specified), configured as a noiseless device. The machine on

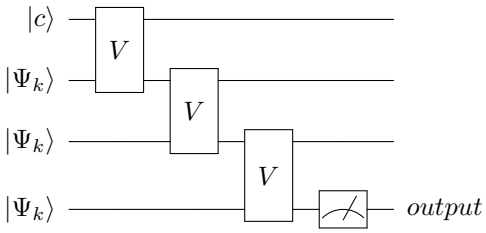

FIGURE 5: This figure depicts a D-CTC simulation for which $N = 3$.

which the backend was installed is equipped with a 24-cores CPU, where each core is an *Intel Xeon Processor* (*Cascade Lake*), and 64 GB RAM.

The thorough performance assessment we carried out required us to simulate a wide range of different scenarios, using both the BHW and NBP models. For this purpose, we realized a Python package built on top of *Qiskit* [15], which abstracts the underlying complexity of the quantum circuits and delivers a simple API to the final user. Fig. 6 shows a simplified version of the interface: we can see that the user has just to initialize an instance of *CTCCircuitSimulator* specifying the number of qubits n and the target state $|k\rangle\langle k|$ through parameters *size* and *k_value* respectively. By setting the parameter *ctc_recipe*, the user chooses which model and which input set to use for the simulation. Results are produced in the form of text files and bar plots just by calling public methods like

- *simulate*, to gather measurement outcomes for the scenario defined by a specified initial state $|c\rangle\langle c|$ (parameter *c_value*);
- *test_convergence*, to test the same scenario under a varying number of iterations (this method is key to determine $N_{land}(95\%)$, and we used it to generate the bar plots reported in the next section);

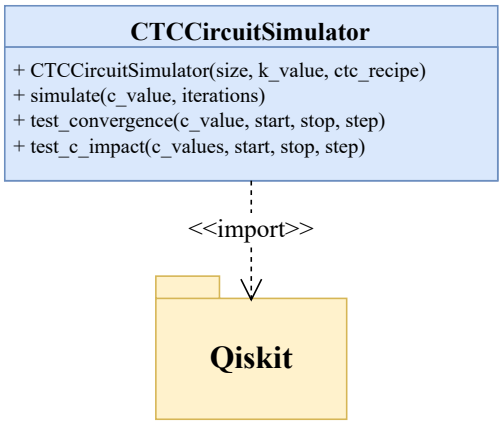

FIGURE 6: A simplified version of the interface of our Python package.

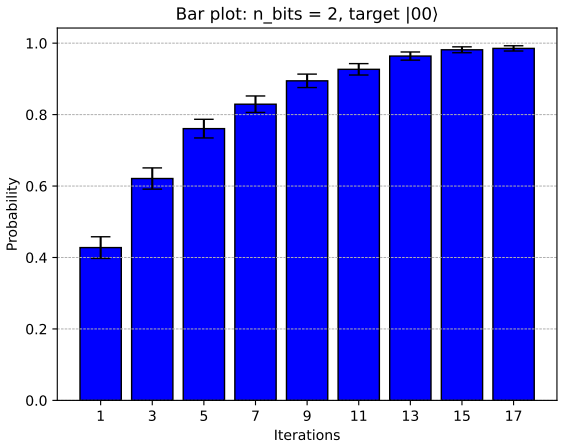

FIGURE 7: BHW bar plot for scenario $(n = 2, |c\rangle = |{+}{+}\rangle, |k\rangle = |00\rangle)$.

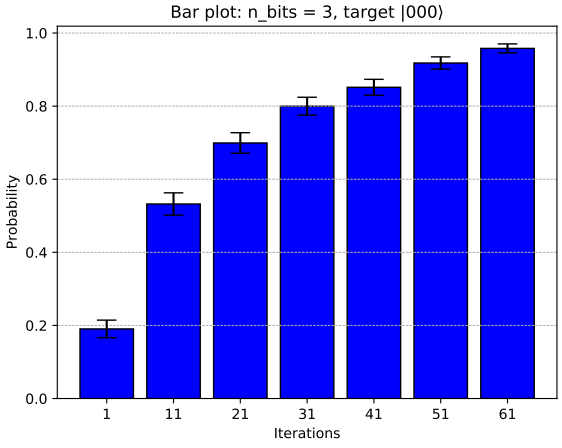

FIGURE 8: BHW bar plot for scenario $(n = 3, |c\rangle = |{+}{+}{+}\rangle, |k\rangle = |000\rangle)$.

- *test_c_impact*, to determine the impact of the initial state $|c\rangle\langle c|$ on $N_{land}(95\%)$.

Since it is computationally hard to execute the BHW quantum circuit in scenarios where $n = 4$, we also developed a Python program relying on *NetSquid* [16]. It realizes an API very similar to the one shown above, but the algorithm numerically computes the output state of the circuit by applying each iteration as a single unitary matrix, without decomposing it in primitive gates.

We make available to interested users the full set of outcome bar plots at [17].

VI. BHW MODEL VS NBP MODEL ASSESSMENT

In this section, we estimate the convergence speed of the BHW and NPB quantum circuits specified above, both powered by the $XZ(n)$-input set (9). Outcomes of our analysis are shown by several bar plots where:

- x-axis reports the number of iterations performed by the simulator.
- y-axis reports, for each iteration, the estimated probability of correct discrimination $p(k, N)$.
- Each bar shows an error edge representing the 95% confidence interval.

Because of space problems, we only report the more significant scenarios in which the initial state $|c\rangle$ is the Hadamard state. We verified through our in-depth simulative analysis that for both BHW/NBP quantum circuits the Hadamard state guarantees the lowest value of $N_{land}(95\%)$ without any a priori knowledge about the state $|\psi_k\rangle$. Obviously, we did not consider scenarios where $|c\rangle = |k\rangle$, because in these cases the system has already converged to the fixed point. See Appendix C for details regarding this topic.

A. BHW QUANTUM CIRCUIT ASSESSMENT

1) Outcomes for n=2 and n=3

Figs. 7 and 8 show the behavior of the convergence speed towards the corresponding fixed points for $n = 2$ and $n = 3$ respectively. From these figures emerges that $N_{land}(95\%) =$ 13 iterations for $n = 2$ whereas $N_{land}(95\%) = 60$ iterations for $n = 3$. This means that with a probability of 0.95, we need 13 and 60 copies of $|\psi_k\rangle$ to discriminate between $2^2 = 4$ non-orthogonal states and $2^3 = 8$ non-orthogonal states respectively. This trend in the increase of N_{land} as n increases, is further confirmed by the outcomes obtained for $n = 4$.

2) Outcomes for n=4

Before showing the results of these scenarios, we need to make it clear that we had to modify the background for our simulations. Since the BHW quantum circuit has a quantum cost in the order of $O(2^n)$ primitive gates (as pointed out in [8]), *Qiskit's transpiler* takes an unacceptable amount of time in decomposing and executing the controlled gates in an equivalent combination of primitive gates. For this reason, we exploited the *NetSquid* [16] framework, which applies those gates as a single matrix, thus drastically reducing the execution time. Fig. 9 clearly shows that, with $n = 4$, $N_{land}(95\%)$ is reached in about 270 iterations. The same

This article has been accepted for publication in a future issue of this journal, but has not been fully edited. Content may change prior to final publication. Citation information: DOI 10.1109/TQE.2022.3142531, IEEE Transactions on Quantum Engineering

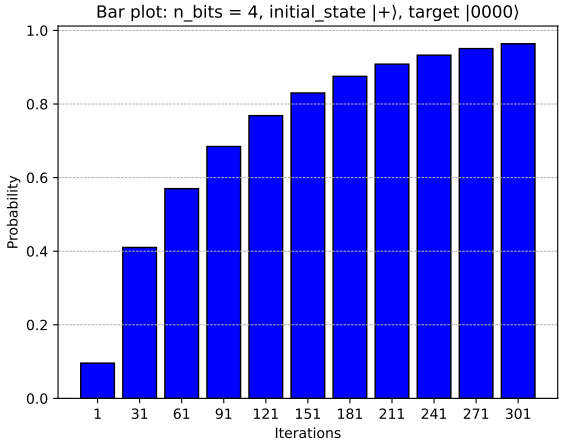

FIGURE 9: BHW bar plot for scenario $(n = 4, |c\rangle = |+\,+\,+\,+\rangle\,, |k\rangle = |0000\rangle)$.

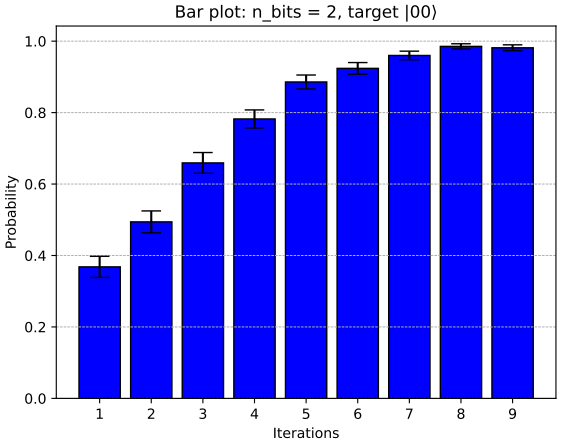

(a)

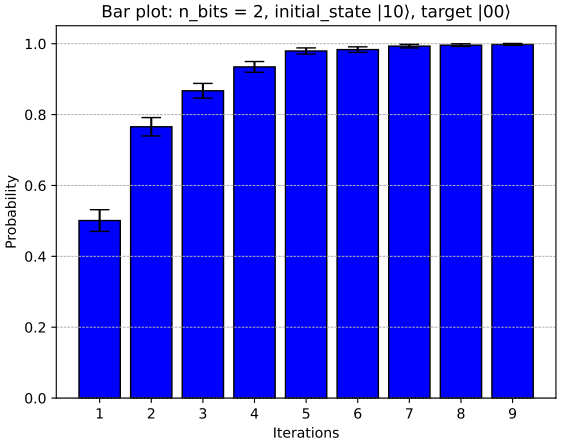

(b)

FIGURE 10: BHW bar plots for scenarios $(n = 2, |c\rangle = |{+}{+}\rangle\,, |k\rangle = |00\rangle)$ (a) and $(n = 2, |c\rangle = |10\rangle\,, |k\rangle = |00\rangle)$ (b), using the alternative set of matrices.

number of iterations would have been achieved if we had used the quantum gates provided by the Qiskit's transpiler, but the time would have been much greater.

3) $\{U_k\}_{k=0}^{2^n-1}$ analysis

The findings reported above are based on the matrices $\{U_k\}_{k=0}^{2^n-1}$ that we derived using the BHW algorithm as it is defined in [6]. Recalling Section III-A, the BHW algorithm entails, for each unitary U_k, the construction of two orthonormal bases $\mathcal{B} = \{|b_1\rangle, \ldots, |b_{2^n}\rangle\}$ and $\mathcal{C} = \{|c_1\rangle, \ldots, |c_{2^n}\rangle\}$. The algorithm imposes a unique way to determine the first two states of each set, i.e. $|b_1\rangle\,, |b_2\rangle\,, |c_1\rangle\,,$ and $|c_2\rangle$. Despite the choice of the remaining basis states ($\{|b_3\rangle \ldots |b_{2^n}\rangle\}$ and $\{|c_3\rangle \ldots |c_{2^n}\rangle\}$) is free, it does not have any impact on the performance of the algorithm (at least) in terms of $N_{land}(95\%)$. To put it another way, giving $|b_1\rangle\,, |b_2\rangle\,, |c_1\rangle\,,$ and $|c_2\rangle$, different choices of $\{|b_3\rangle \ldots |b_{2^n}\rangle\}$ and $\{|c_3\rangle \ldots |c_{2^n}\rangle\}$ lead to the same $N_{land}(95\%)$. This surprising property (at least at first sight) of bases $\mathcal{B}$ and $\mathcal{C}$ was subjected to a comprehensive verification (for $n = 2, 3$) by simulation. However, there is still considerable freedom in choosing the algorithm used to build $\{U_k\}_{k=0}^{2^n-1}$, whose only constraints are represented by (7) and (8). For example, an alternative to the BHW algorithm may exploit a different approach for the construction of $|b_1\rangle\,, |b_2\rangle\,, |c_1\rangle$ and $|c_2\rangle$, leading to different performance.

In fact, Brun *et al.* in [6] present an alternative set of matrices for the $n = 2$ scenario, which still comply with the sufficient conditions in (7) and (8). Fig. 10a shows that using this specific set, $N_{land}(95\%)$ is reached with certainty after just 7 iterations (using Hadamard as initial state), which is about half of the 13 iterations needed for the scenario in Fig. 7. The scenario which led to the bar plot in Fig. 10b performs particularly well and leads to an insight which will be detailed in Section VII-C.

Therefore, the lesson learned is that the choice of matrices $\{U_k\}_{k=0}^{2^n-1}$ can have a significant impact on $N_{land}(95\%)$. We will delve deeper into this topic in Section VII-C. Henceforth, we will continue to use $\{U_k\}_{k=0}^{2^n-1}$ obtained using the algorithm shown in Fig. 3, being aware that there may be alternative choices performing better or worse. The problem of finding the set of matrices $\{U_k\}_{k=0}^{2^n-1}$ that minimizes the value of $N_{land}(95\%)$ remains an open issue which can be the topic of another potential paper.

4) BHW Assessment Considerations

Fig. 11 reports $N_{land}(95\%)$ for $n = 2, 3, 4$. The purpose of this figure is to emphasize that the value of $N_{land}(95\%)$ appears to be in the order of $O(2^{2n})$, at least for the scenarios considered in this analysis.

For completeness, Table I (and Table II, see below) shows the time to execute $N_{land}(95\%)$ iterations in the different scenarios when $n = 2, 3, 4$. Of course, the execution time for $n = 4$ is much shorter as we have moved to a different backend. For each n, the computation was performed using

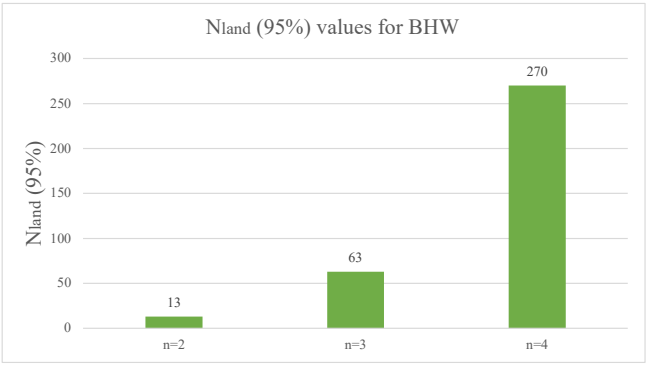

FIGURE 11: A summary bar plot showing the value of $N_{land}(95\%)$ as a function of n.

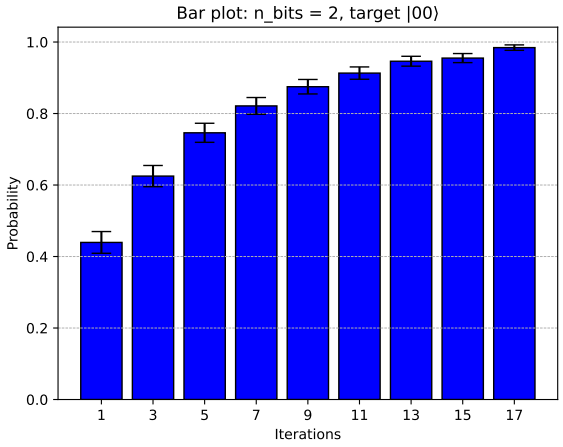

FIGURE 12: NBP bar plot for scenario $(n = 2, |c\rangle = |{+}{+}\rangle, |k\rangle = |00\rangle)$.

the *QasmSimulator* 1024 times (shots) (and *NetSquid* when $n = 4$) running on the equipment described in Section V.

TABLE I: Execution time for 1024 shots of $N_{land}(95\%)$ iterations for $n = 2, 3, 4$.

	Iterations	Time (s)	Backend
n=2	13	43.71862	*QasmSimulator*
n=3	63	6310.75999	*QasmSimulator*
n=4	270	1.21239	*NetSquid*

B. NBP QUANTUM CIRCUIT ASSESSMENT

Figs. 12, 13 and 14 represent, for the NBP model, the corresponding Figs. 7, 8 and 9 for the BHW model.

When we compare these bar plots of both models with the same n, we notice that the BHW model reaches the fixed point slightly (between 7% and 11%) faster than the NBP model.

Since the NBP model has an efficient quantum cost which is in the order of $O(n)$, the fixed point was achieved in a reasonable time using *Qiskit Aer QasmSimulator* for all scenarios.

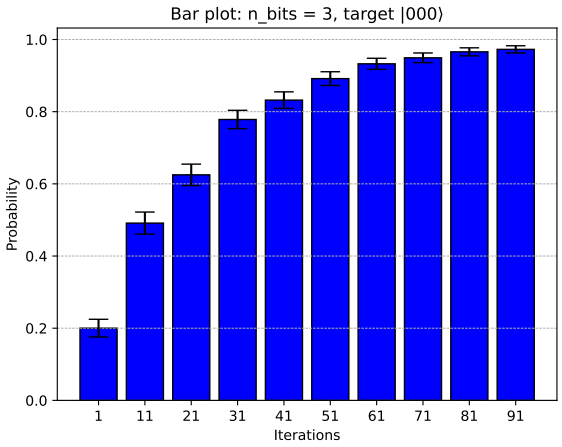

FIGURE 13: NBP bar plot for scenario $(n = 3, |c\rangle = |{+}{+}{+}\rangle, |k\rangle = |000\rangle)$.

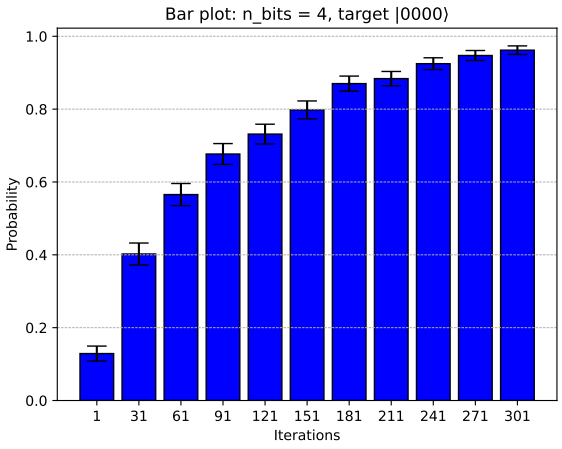

FIGURE 14: NBP bar plot for scenario $(n = 4, |c\rangle = |{+}{+}{+}{+}\rangle, |k\rangle = |0000\rangle)$.

1) NBP Assessment Considerations

Fig. 15 shows that the exponential relationship between n and $N_{land}(95\%)$ still holds for the NBP model. Table II reports the execution times for $n = 2, 3, 4$. From a simulation point of view, it should be pointed out that the $O(n)$ cost of the NBP model leads to a drastic reduction in the total number of quantum gates applied to run $N_{land}(95\%)$ iterations w.r.t. the BHW model, whose cost is $O(2^n)$.

This article has been accepted for publication in a future issue of this journal, but has not been fully edited. Content may change prior to final publication. Citation information: DOI 10.1109/TQE.2022.3142531, IEEE Transactions on Quantum Engineering

TABLE II: Execution time for 1024 shots of $N_{land}(95\%)$ iterations for $n = 2, 3, 4$.

	Iterations	Time (s)	Backend
n=2	14	0.40567	*QasmSimulator*
n=3	70	2.08098	*QasmSimulator*
n=4	295	9.99327	*QasmSimulator*

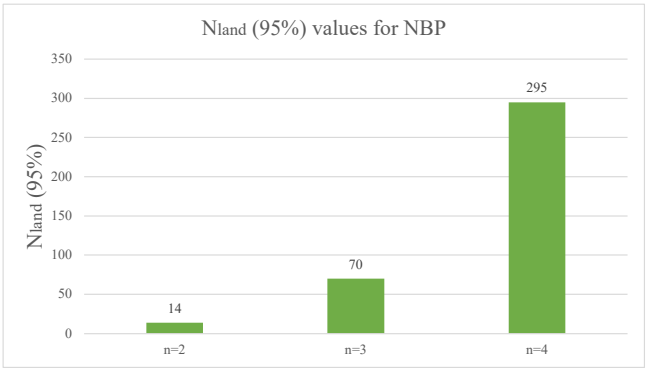

FIGURE 15: A summary bar plot showing the value of $N_{land}(95\%)$ as a function of n.

VII. IMPACT OF THE INPUT SET ON CONVERGENCE

The performance analysis shown so far has exploited the $XZ(n)$-input set, i.e. a set of non-orthogonal pure states (9) evenly spaced on the XZ-plane of the Bloch sphere. The main advantage of the $XZ(n)$-input set is that all states belonging to it can easily be obtained through simple rotations along the Y axis of the Bloch sphere. This advantage was largely exploited by the NBP model illustrated in Section III-B. On the other hand, it is the source of a significant drawback, since forcing all states to lie on the XZ-plane of the Bloch sphere, it leads to great overlap between states, making their discrimination hard. Fig. 16 shows this situation. The above considerations have led us to deepen our understanding of the relationship between the overlap among the non-orthogonal states of an input set and $N_{land}(95\%)$. Specifically, given a generic input set of K non-orthogonal states to be discriminated, we want to tackle the following problems:

- Can one characterize their overlap with the value of a "collective" metric?
- Does the metric values have a relationship with $N_{land}(95\%)$?

These questions will be answered in sequence.

A. THE QUANTUM CHERNOFF BOUND METRIC

Our choice to tackle the first problem is the quantum Chernoff bound (hereafter QCB) because of its nice feature of universality, as it identifies the unique metric quantifying the distance of quantum states that does not share the undesirable features of other distance measures like the fidelity, the trace norm and the relative entropy [18]. Appendix A sketches the QCB and provides some references for the reader who wants to delve deeper into this topic.

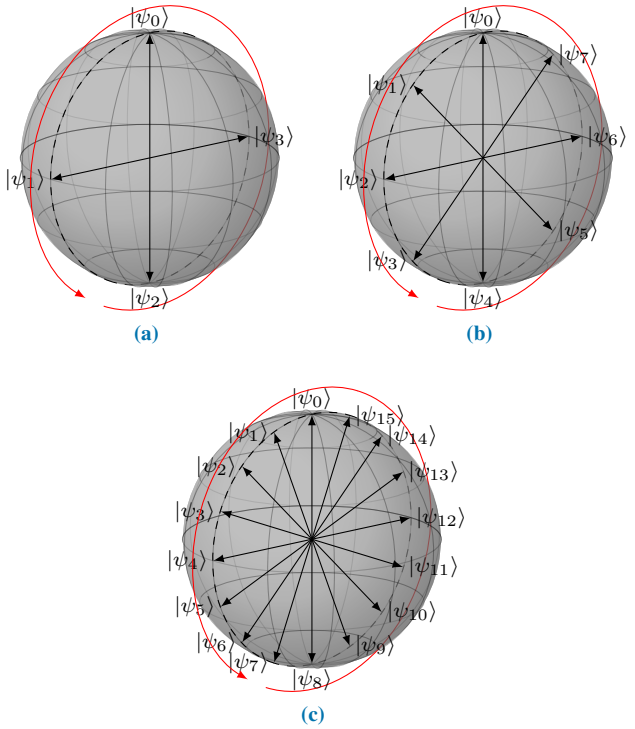

FIGURE 16: *XZ(n)* states represented on the Bloch sphere, for (a) $n = 2$, (b) $n = 3$, (c) $n = 4$. Note that they are confined on the XZ-plane.

B. DIFFERENT INPUT SETS DEFINITION

To quantify the impact of an input set on its QCB and on $N_{land}(95\%)$ we need to define different input sets according to criteria that help us to unearth the aforementioned relationship. The approach we have pursued hinges on several input sets with their states located at the vertices of polygons (2D) and polyhedrons (3D), not always regular, both inscribed in the Bloch sphere.

1) *XZ(n)*-input set

This is a set of equidistant states on the XZ plane of the Bloch sphere. These states are arranged at the vertices of a regular polygon inscribed in the XZ-plane circumference of the Bloch sphere as shown in Fig. 16. For $n = 2$ we have four states located at the vertices of a square, for $n = 3$ we have eight states located at the vertices of an octagon, etc. This arrangement achieves the maximum QCB for states bound to the same plane. We have already defined this set in Section III-B and exploited this scenario in Section VI.

2) *XZ(n, ϕ)*-input set

This is a set of states fairly distributed on a Bloch sphere meridian identified by an angle ϕ. This input set is obtained by rotating the $XZ(n)$-input set of an angle ϕ around the z-axis. Formally:

$$|\psi_k\rangle = \cos\frac{\pi k}{2^n}|0\rangle + e^{i\phi}\sin\frac{\pi k}{2^n}|1\rangle \qquad (14)$$

TABLE III: $XYZ(n=2)$ encoding map.

$\|\psi_0\rangle$	$\|0\rangle$
$\|\psi_1\rangle$	$\cos 0.3041\pi \|0\rangle + \sin 0.3041\pi \|1\rangle$
$\|\psi_2\rangle$	$\cos 0.3041\pi \|0\rangle + e^{i\frac{2\pi}{3}} \sin 0.3041\pi \|1\rangle$
$\|\psi_3\rangle$	$\cos 0.3041\pi \|0\rangle + e^{-i\frac{2\pi}{3}} \sin 0.3041\pi \|1\rangle$

This input set will allow us to check whether the angle ϕ has an influence on $N_{land}(95\%)$ when we turn around the z-axis the plane on which the states are located.

3) *XZ(n, quadrant)* Input Set

This set of inputs is obtained by taking the states of the $XZ(n)$-input set and distributing them uniformly across one quadrant of the XZ plane. Formally,

$$|\psi_k\rangle = \cos\frac{\pi k}{2^{n+2}}|0\rangle + \sin\frac{\pi k}{2^{n+2}}|1\rangle \tag{15}$$

The rational behind this choice is that qubit states are now closer to each other with respect to the $XZ(n)$-input set and therefore their overlap increases.

4) *XYZ(n)*-input set

In order to separate spatially the various states of an input set, so as to maximize the set's QCB, we place the states at the vertices of regular polyhedrons inscribed in the Bloch sphere. The resulting input set $\{|\psi_k\rangle\}_{k=0}^{2^n-1}$ will be termed $XYZ(n)$-input set where n is such that 2^n gives the number of the quantum states to be discriminated.

XYZ(n=2) - We define this input set by picking four states placed at the vertices of an ideal tetrahedron inscribed in the Bloch sphere. Table III reports the formal definition of the states, which are geometrically represented in Fig. 17a.

XYZ(n=3) - In this input set each state is associated to a vertex of a cube ($n=3$, and therefore $2^3=8$) inscribed in the Bloch sphere. Table IV reports the eight state vectors, and Fig. 17b represents them on the sphere.

XYZ(n=4) - Unfortunately, there is no regular polyhedron having sixteen vertices. For this reason, we propose to use an approximate polyhedron by exploiting a method which can easily be generalized to any value of n:

- Draw two meridians on the Bloch sphere corresponding to $\varphi = 0, \frac{\pi}{2}$.
- Draw four parallels on the Bloch sphere corresponding to $\theta = \frac{\pi}{5}, \frac{2\pi}{5}, \frac{3\pi}{5}, \frac{4\pi}{5}$.
- The states that make up the encoding are the sixteen intersections of these parallels and meridians. We rely on Fig. 17c for a graphic representation.

5) *XYZ(n, clove)*-input set

Like we did for the $XZ(n, quadrant)$-input set, here we redistribute the states of the $XYZ(n)$-input set equally on a reduced clove of the Bloch sphere, identified by $\theta \in [0, \frac{\pi}{2}]$ and $\phi \in [0, \pi]$. The aim of this input set is to increase the overlap among its states w.r.t. $XYZ(n)$, which in turn should make their discrimination more difficult. There are several ways to achieve this purpose, each characterized by its own QCB. Since, in doing this, we did not commit ourselves to any optimization problem, we decided to distribute the states on the clove uniformly on the meridians and the parallels, i.e. in the most basic way, according to the following algorithm.

- For $n=2$ we place $|\psi_0\rangle$, $|\psi_1\rangle$ and $|\psi_3\rangle$ on half of the XZ-plane. The $|\psi_2\rangle$ state is obtained by rotating $|\psi_0\rangle \equiv |0\rangle$ by 90 degrees on the YZ-plane. See Fig. 18a.
- For $n=3$ we drew an intermediate semi-parallel on the clove, identified by $\theta = \pi/4$. We placed three states ($|\psi_5\rangle$, $|\psi_6\rangle$ and $|\psi_7\rangle$) uniformly spread over this semi-parallel, four states ($|\psi_1\rangle$, $|\psi_2\rangle$, $|\psi_3\rangle$, $|\psi_4\rangle$) uniformly spread over half of the XZ-plane, and finally a state $|\psi_0\rangle \equiv |0\rangle$. See Fig. 18b.
- For $n=4$ we used an approach very similar to the $n=3$ case, i.e. we drew two intermediate semi-parallels at $\theta = \pi/6, \pi/3$. We uniformly placed three and five states on these semi-parallels respectively, seven states on half of the XZ-plane and again $|\psi_0\rangle \equiv |0\rangle$. See Fig. 18c.

In Fig. 18a we highlight a strong resemblance with BB84

TABLE IV: $XYZ(n=3)$ encoding map.

$\|\psi_0\rangle$	$\cos 0.1521\pi \|0\rangle + \sin 0.1521 \|1\rangle$
$\|\psi_1\rangle$	$\cos 0.1521\pi \|0\rangle + i \sin 0.1521 \|1\rangle$
$\|\psi_2\rangle$	$\cos 0.1521\pi \|0\rangle - \sin 0.1521 \|1\rangle$
$\|\psi_3\rangle$	$\cos 0.1521\pi \|0\rangle - i \sin 0.1521 \|1\rangle$
$\|\psi_4\rangle$	$\cos 0.3480\pi \|0\rangle + \sin 0.3480\pi \|1\rangle$
$\|\psi_5\rangle$	$\cos 0.3480\pi \|0\rangle + i \sin 0.3480\pi \|1\rangle$
$\|\psi_6\rangle$	$\cos 0.3480\pi \|0\rangle - \sin 0.3480\pi \|1\rangle$
$\|\psi_7\rangle$	$\cos 0.3480\pi \|0\rangle - i \sin 0.3480\pi \|1\rangle$

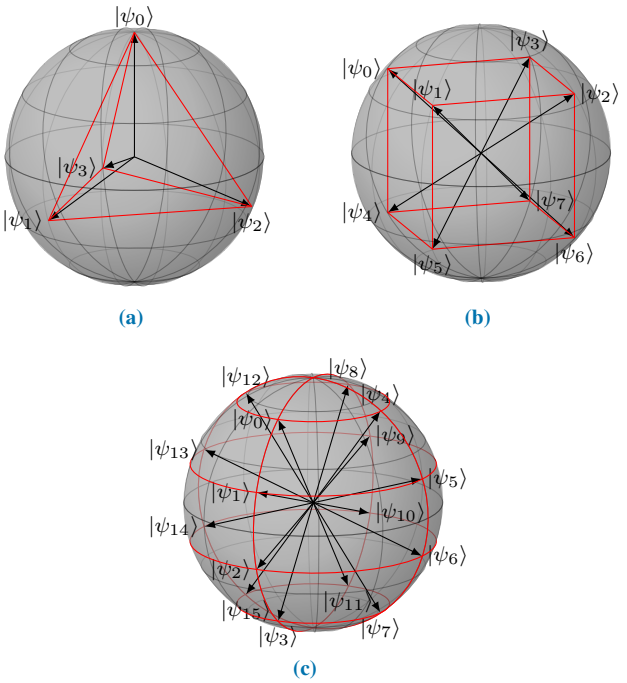

FIGURE 17: *XYZ(n)* states represented on the Bloch sphere, for (a) $n=2$, (b) $n=3$, (c) $n=4$. Note that they exploit all the 3d space of the sphere.

TABLE V: QCB values for the input sets we defined, depending on the number of bits n.

	XZ(n, quadrant)	*XZ(n)*	*XZ(n, ϕ)*	*XYZ(n, clove)*	*XYZ(n)*
n=2	0.03880	0.69315	0.69315	0.69315	1.09860
n=3	0.00965	0.15835	0.15835	0.15835	0.40541
n=4	0.00241	0.03880	0.03880	0.06933	0.10036

states, the only topological difference is that $|\psi_2\rangle$ is rotated by 90 degrees on the YZ-plane. In Fig. 18b we point out that the states $|\psi_4\rangle, |\psi_7\rangle, |\psi_0\rangle, |\psi_5\rangle, |\psi_1\rangle$, are placed on half of the XZ-plane, exactly like the first five states from $XZ(n = 3)$. These considerations justify the fact that $XZ(n)$ and $XYZ(n, clove)$ share the same QCB if $n = 2$ or $n = 3$.

To clarify further the relationship between the level of overlap of the states that comprise the previously defined input sets and their QCBs, it may be helpful to be aware of the QCB values associated with the corresponding input sets. Table V reports, for any input set defined above, the value of the QCB for $n = 2, 3, 4$. The table clearly indicates that the QCB values are consistent with the overlapping state considerations. Specifically,

- $XZ(n, quadrant)$-input sets have QCB values well below those of other input sets.
- $XZ(n)$- and $XZ(n, \phi)$-input sets share the same quantum states topology on the Bloch sphere. As a result, they have the same QCB value, regardless of ϕ.
- $XYZ(n)$-input sets have significantly higher QCB values than those pertaining to the other input sets thanks to the tri-dimensional redistribution of states which lowers the overlap.
- The $XYZ(n, clove)$-input sets have the same QCB values as the $XZ(n)$-input sets in which $n = 2$ and $n = 3$.
- Although the $XYZ(n, clove)$ and $XZ(n, quadrant)$ input sets are defined with the purpose to increase the overlap between states, the former has a far higher QCB than the latter. This may be justified geometrically along the following lines of reasoning. In $XYZ(n, clove)$, the states can be spread over a quarter of the surface of the Bloch sphere so that they have fewer opportunities for overlap than in the $XZ(n, quadrant)$ in which states can be distributed over the arc of a quadrant of a unit circle. Consequently, the QCB of $XYZ(n, clove)$ is significantly less than the QCB of $XZ(n, quadrant)$.

C. EVALUATION OF THE INPUT SETS

By design, the NBP model can only support $XZ(n)$ as input sets. Therefore, the following analysis pertains exclusively to the BHW model that supports all types of input sets. As discussed in Section III-A, each input set gives rise to a specific BHW circuit which can be determined using the BHW algorithm.

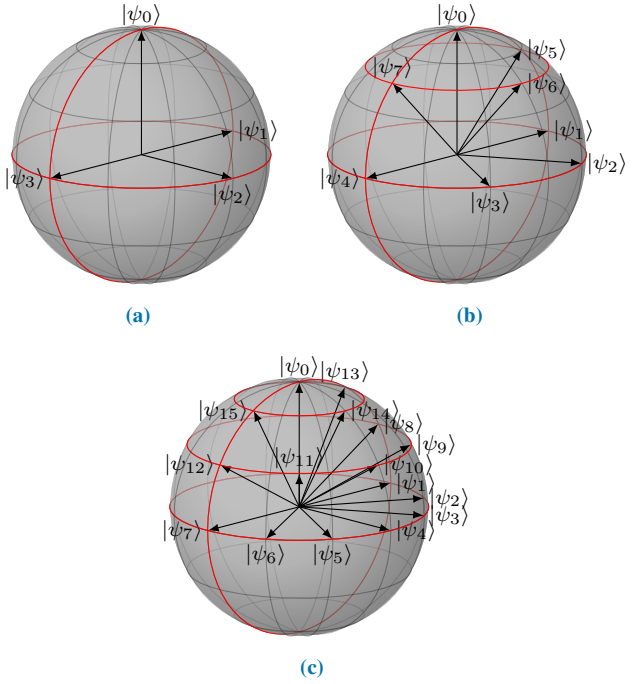

FIGURE 18: *XYZ(n, clove)* states represented on the Bloch sphere, for (a) $n = 2$, (b) $n = 3$, (c) $n = 4$. Note that they are bound to one fourth of the sphere.

In the following, we quantify the impact of QCB values on $N_{land}(95\%)$. For this purpose, we applied the simulative approach described in Section IV and determined the $N_{land}(95\%)$ for each input set.

Fig. 19 clearly highlights that there is a strong correlation between the value of QCB and that of $N_{land}(95\%)$. This correlation tends to grow even more when there are more states. We can indeed notice how the gap between the $N_{land}(95\%)$ values of $XZ(n, quadrant)$-, $XZ(n)$- and $XYZ(n)$-input sets become much greater when we raise the value of n.

A further consideration can be made regarding input sets with the same QCB value. Taking $XZ(n)$ and $XYZ(n, clove)$ for $n = 2$ and $n = 3$, we note that, from the $N_{land}(95\%)$ standpoint, the latter (see Fig. 19) performs slightly worse than the former.

Lastly, we found out from comparing Fig. 7 and Fig. 10 pertaining to $XZ(2)$ that there is plenty of room for improvement in Brun *et al.* algorithm. We therefore took a closer look at Fig. 10b in order to better understand how $p(k, N)$ evolves as the number of iterations N increases. By using *Python scipy 1.7.1* we discovered that the best fit of the bar plot of Fig. 10b is

$$f(N) = 1 - \exp\{-\gamma N\} \tag{16}$$

where N is the iteration number and $\gamma = 0.69315$, which is exactly the Chernoff bound! (as reported in Table V).

Now, if we assume that (16) holds also for the other scenarios, then we could draw the bar plot reported in Fig.

19 where the height of the dark green bars is equal to $N_{land}(95\%)$ whereas the height of the light green bars, denoted by $N_{QCB}(95\%)$, is calculated as follows.

$$N_{QCB}(95\%) = \min_{N}\{N : 1 - \exp\{-N\xi^{S}_{QCB}\} \geq 0.95\}, \tag{17}$$

where ξ^{S}_{QCB} is the QCB of the corresponding input set S (see Appendix A). In other words, if it were possible to design an algorithm (hereinafter referred to as AQCB) capable of achieving the QCB limit for any input set, then the BHW enhancement margin with respect to the AQCB would be accurately quantified by the difference between the light green and dark green bar heights in Fig. 19. This means that a recipe to build the unitaries $\{U_k\}_{k=0}^{2^n-1}$ different from the one described by the algorithm in Fig. 3 could lead to much better results, and the proof of this statement is the alternative set of matrices shown in Section VI-A3. Finally, we conclude this section with the definition of a new metric that enabled us to enrich the assessment carried out thus far.

Indeed, Fig. 19 also reports (orange dots) the ratio of the minimum number of iterations $N_{QCB}(95\%)$ as predicted by the AQCB algorithm to the observed values of $N_{land}(95\%)$ of the BHW algorithm. This performance index reflects BHW's performance against AQCB in relative terms rather than absolute terms, as $N_{QCB}(95\%)$ or $N_{land}(95\%)$ have done.

This ratio is 1 when the two algorithms perform equally and approaches 0 when the AQCB outperforms BHW.

VIII. CONCLUSIONS AND OUTLOOK

In this paper, we performed a thorough simulative analysis of two quantum circuits from [6] and [8], which discriminate non-orthogonal quantum states with the assistance of D-CTCs. Our analysis boils down to evaluating a convergence speed towards a fixed point when the above quantum circuits are fed with specific input sets comprising non-orthogonal states.

Results clearly show that, when both models are fed with an $XZ(n)$-input set (the only possible input set for a comparison) with a number of states greater than 4 ($n = 2$), the number of iterations required to achieve perfect discrimination may be too high to be helpful in practical applications.

For the Brun *et al.* [6] model only, another finding is that the number of iterations needed to reach the fixed point depends heavily on the input set supplied to the model. In particular, Fig. 19 points out that the input set $XYZ(n)$ outperforms with respect to the input set $XZ(n, quadrant)$.

Through our in-depth simulative analysis, we found that the above dependency is closely related to the degree of overlap between states within the input set. To quantify this dependence, we exploited the quantum Chernoff bound metric to characterize the non-orthogonality of the states within an input set and this enabled us to figure out how the bigger the QCB the smaller the $N_{land}(95\%)$.

Finally, for both models, a significant burden is that an original copy of the qubit state is required for each iteration.

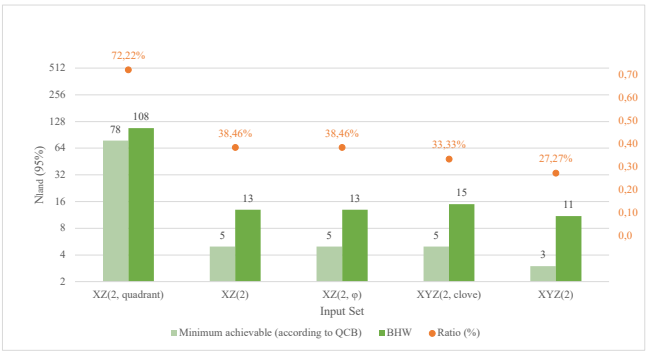

(a)

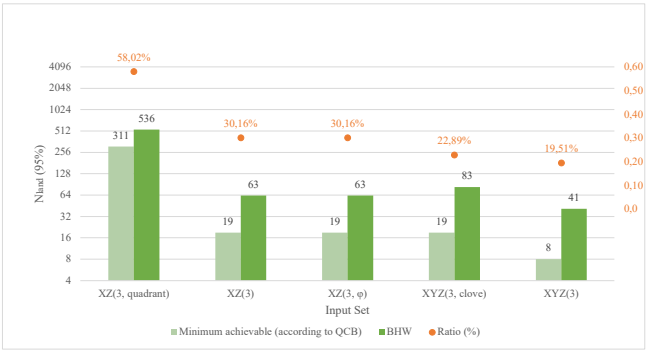

(b)

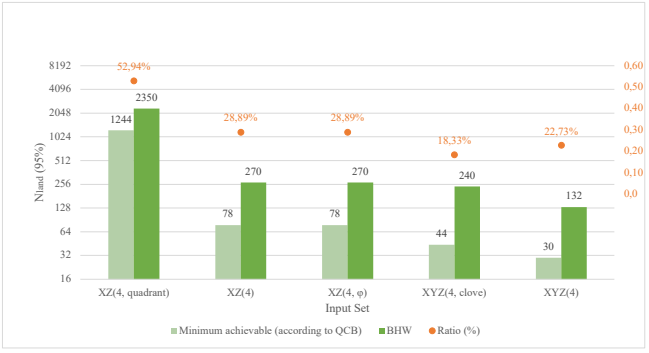

(c)

FIGURE 19: Bar plots showing $N_{land}(95\%)$ depending on the input sets we defined, for $n = 2$ (a), $n = 3$ (b) and $n = 4$ (c). Dark green bars report $N_{land}(95\%)$ for the BHW algorithm, whereas light green bars report $N_{QCB}(95\%)$.

This fact and the high value of $N_{land}(95\%)$, even if n is small, does not allow, for example, to use a qubit to convey classic Internet packets (i.e. a string of hundreds of bits) from the sender to the recipient. Let us consider the simplest case, that is $n = 2$. The sender encodes the qubit and teleports it to the receiver which will have to decode it. Using the most performing BHW quantum circuit, it takes 7 iterations to extract two bits with a probability of 95%. This means that we should use 7 copies of the qubit to extract, with a 95% probability, 2 classical bits. However, we know that with the superdense coding [19], with probability 1, we can extract 2 classical bits from one qubit. As a conclusion, despite that with a CTC assisted quantum circuit the Holevo

bound is violated, superdense coding still remains the most effective approach for moving classical bits along a quantum communication channel.

In an attempt to eliminate the use of one copy of the original qubit for every iteration we also tested the use of approximate cloned copies [20] of the original qubit. Unfortunately, the results were disappointing, and we gave up on that approach.

However, we now have figures that allow us to compare the BHW and NBP quantum circuits against the performance of existing algorithms that use constant-sized quantum memory [21]. This topic has been left for a next potential paper. Furthermore, as we discussed in Section VII-C, the recipe used to build U_k matrices has a significant impact on the performance of the discrimination algorithm. Thus, the problem of finding the $\{U_k\}_{k=0}^{K-1}$ set that minimizes the value of $N_{land}(95\%)$ is an open issue that deserves to be addressed.

APPENDIX. A

In the following we sketch the reasoning which led to the QCB. Let ρ_1 and ρ_2 be two quantum states and denote by $\rho_1^{\otimes N}$ and $\rho_2^{\otimes N}$ the quantum states composed of N *i.i.d.* copies of ρ_1 and ρ_2 respectively. A party prepares a quantum system in a state either $\rho_1^{\otimes N}$ or $\rho_2^{\otimes N}$. The optimal success probability $p_{success,N}$, for a second party to guess which of these two states has been prepared is fully described by the Helstrom bound [22], which exploits the trace distance between the two states. It is however not straightforward to compute the trace distance between *i.i.d.* states $\rho_1^{\otimes N}$ and $\rho_2^{\otimes N}$ in an analytic form. Furthermore, the Helstrom bound cannot be generalized to a set with multiple states. However, if N is large enough, the optimal success probability can be approximated as $p_{success,N} \approx 1 - \exp\{-N\xi_{QCB}\}$, where the quantity ξ_{QCB} is called quantum Chernoff bound (QCB for short), and is computed as (from [18])

$$\begin{aligned}\xi_{QCB} &= \lim_{N\to\infty} -\frac{1-p_{success,N}}{N} = \\ &= -\log\left(\min_{0\le s\le 1} \mathrm{Tr}\{\rho_1^s \rho_2^{1-s}\}\right).\end{aligned} \tag{18}$$

Since we are interested in discriminating non-orthogonal states of an input set with multiple states $\{\rho_i\}_{i=1}^{2^n}$, (18) has been extended to the set $S = \{\rho_i\}_{i=1}^{2^n}$ as follows:

$$\xi_{QCB}^S = \min_{i,j} \xi_{QCB}(\rho_i, \rho_j), \quad i,j \in \{1,2,\ldots,2^n\}. \tag{19}$$

This expression involves the pairwise QCB among all pairs. With this generalization, we can apply (19) to any input set of non-orthogonal states and find the related ξ_{QCB}^S.

In this paper we use the term quantum Chernoff bound (or QCB) also for its generalization (19). In literature, it is also commonly referred as multiple Chernoff bound to differentiate it from the pairwise version (18).

APPENDIX. B

As one may have already noticed, the size of the D-CTC simulation circuit grows linearly with the number of iterations N. In particular, if k is the value associated to an n-bit string and we want to perform N iterations, the total number of qubits required by the simulator is

$$\#qubits = (N+1)n. \tag{20}$$

In our case, we experimentally assessed that both IBM-Q *ibmq_qasm_simulator* and *Qiskit Aer QasmSimulator* struggle when the number of qubits exceeds 20. This is a very strict limit to our purposes because the number of iterations that we can test is very low. For example, if $n = 2$, then we can test no more than 9 iterations. If instead $n = 4$, then we can only test up to 4 iterations, which is unacceptable.

Notice that with the D-CTC simulative approach shown in Section IV, quantum registers are "wasted" after the V gate has been applied to them, and new quantum wires are added for the next iteration. We found an optimization which "recycles" these qubits by re-initializing them into a fresh copy of CR system. As we can see in Fig. 21, this is performed by *Reset* operators, indicated by the symbol $|0\rangle$, and initialization gates ($INIT(|\psi_k\rangle)$), which map the state $|0\rangle$ into the encoded state $|\psi_k\rangle$. This approach makes the circuit size independent of the number of iterations N, so that the total number of qubits is always

$$\#qubits = 2n. \tag{21}$$

Fig. 21 shows the case for $n = 2$. The generalization for n-bits is straightforward, as the only thing to do is to add *SWAP* and *Reset* gates to match the size of n.

APPENDIX. C

In this appendix we try to justify our guess that, though based on a large simulation campaign (with all the limitations that simulation implies), the Hadamard state is the initial state that guarantees the best performances in terms of $N_{land}(95\%)$.

For what concerns the XZ-input set, Figs. 20a and 20b clearly show that certain CBS states provide an initial "boost" to the algorithm convergence. In particular, we discovered that for both BHW and NBP (using the XZ-input set) the best CBS initial state $|c\rangle$ is equal to the target state $|k\rangle$ except for the most significant qubit, which is flipped. This can be expressed as

$$|c\rangle = \left|k + 2^{n-1} \mod 2^n\right\rangle. \tag{22}$$

The problem is that we do not have any *a priori* knowledge about the target state $|k\rangle$. It therefore seems reasonable to select an initial state $|c\rangle$ that does not stick to a specific target state $|k\rangle$.

The Hadamard state $|+\rangle^{\otimes n}$ is a perfectly fair superposition of all CBS states. Results show that for the BHW algorithm, it guarantees higher performances than any $|c\rangle \neq |k\rangle$ belonging to the CBS. This still holds true true for all possible input sets we defined, as confirmed by the representative examples shown in Figs. 20a and 20c.

Regarding the NBP algorithm, the Hadamard state remains a better choice than any random CBS state. As shown in Fig.

20b, the performance achieved using $|c\rangle = |{+}{+}\rangle$ is only slightly worse than the best CBS initial state. This was also confirmed in all other scenarios.

The reason why Hadamard performs so well may be explained by the following consideration: since it is a fair superposition, it can't be orthogonal to the target state $|k\rangle$. This guarantees that the algorithm always starts up with a $1/\sqrt{2^n}$ fraction of the state already landed on the fixed point $|k\rangle$.

For input sets having a regular geometric structure like $XZ(n)$ and $XYZ(n)$ our guess is that the Hadamard state is the optimal choice. For other highly non-regular input sets where some states are significantly more "isolated" than others, we saw that BHW algorithm can have very different performances depending on the initial and target states [17]. In such cases, it may be worth exploring the behavior of an initial state $|c\rangle$ built as a weighted superposition of CBS states, where states with worse performances have an increased weight, to speed up the worst case convergence speed.

REFERENCES

[1] D. Deutsch, "Quantum mechanics near closed timelike lines," Phys. Rev. D, vol. 44, pp. 3197–3217, Nov 1991.

[2] T. A. Brun and M. M. Wilde, "Simulations of Closed Timelike Curves," Foundations of Physics, vol. 47, p. 375–391, Jan 2017.

[3] D. Bacon, "Quantum computational complexity in the presence of closed timelike curves," Phys. Rev. A, vol. 70, p. 032309, Sep 2004.

[4] S. Aaronson and J. Watrous, "Closed timelike curves make quantum and classical computing equivalent," Proceedings of the Royal Society A: Mathematical, Physical and Engineering Sciences, vol. 465, p. 631–647, Nov 2008.

[5] J. L. Pienaar, T. C. Ralph, and C. R. Myers, "Open timelike curves violate heisenberg's uncertainty principle," Phys. Rev. Lett., vol. 110, p. 060501, Feb 2013.

[6] T. A. Brun, J. Harrington, and M. M. Wilde, "Localized closed timelike curves can perfectly distinguish quantum states," Phys. Rev. Lett., vol. 102, May 2009.

[7] J. Bae and L.-C. Kwek, "Quantum state discrimination and its applications," Journal of Physics A: Mathematical and Theoretical, vol. 48, p. 083001, Jan 2015.

[8] H. R. Nareddula, B. K. Behera, and P. K. Panigrahi, "Quantum cost efficient scheme for violating the Holevo bound and cloning in the presence of Deutschian closed timelike curves," 2018. arXiv:1901.00379.

[9] L. Bacciottini, "Encoding and extracting a classical internet packet from a qubit: issues, algorithms and their performance evaluation," Master's thesis, University of Pisa, https://etd.adm.unipi.it/theses/browse/by_author/b.html or https://drive.google.com/file/d/1q9crwuFjhRLs0RAQ801SUbFQnCObJqlG/view, Sep 2021.

[10] M. A. Nielsen and I. L. Chuang, Quantum Computation and Quantum Information: 10th Anniversary Edition. USA: Cambridge University Press, 10th ed., 2011.

[11] T. C. Ralph and C. R. Myers, "Information flow of quantum states interacting with closed timelike curves," Physical Review A, vol. 82, Dec 2010.

[12] A. S. Holevo, "Bounds for the quantity of information transmitted by a quantum communication channel," Problems of Information Transmission, vol. 9, no. 3, pp. 177–183, 1973.

[13] A. K. Goswami and P. K. Panigrahi, "Quantum coherence and Holevo bound," 2017. arXiv:1703.08700.

[14] E. Bernstein and U. Vazirani, "Quantum complexity theory," SIAM J. Comput., vol. 26, pp. 1411–1473, Oct 1997.

[15] Qiskit, "Qiskit, Open Source Quantum Development." https://qiskit.org/. Last accessed: 15 Nov 2021.

[16] Netsquid, "Netsquid." https://netsquid.org. Last accessed: 17 Nov 2021.

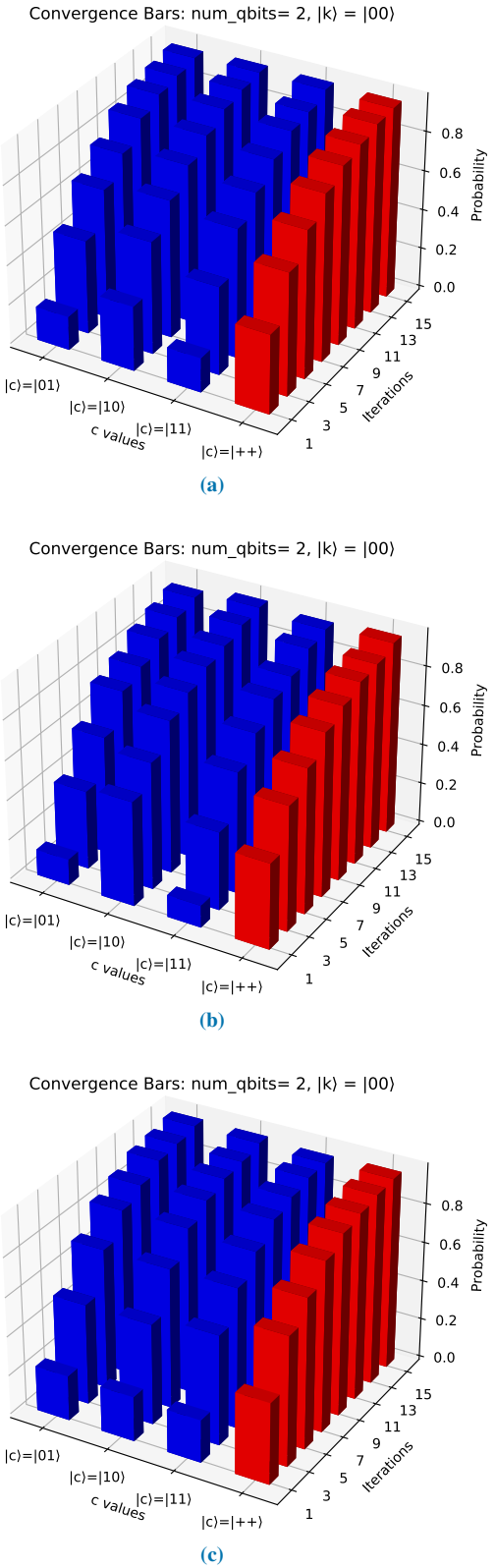

FIGURE 20: Bar plots showing how the choice of a different initial state $|c\rangle$ impacts on the performance of the BHW algorithm with XZ-input set (a), NBP algorithm (b) and BHW algorithm with XYZ-input set (c). Blue bars regard initial states picked from the CBS, whereas red bars show the performance of the Hadamard initial state.

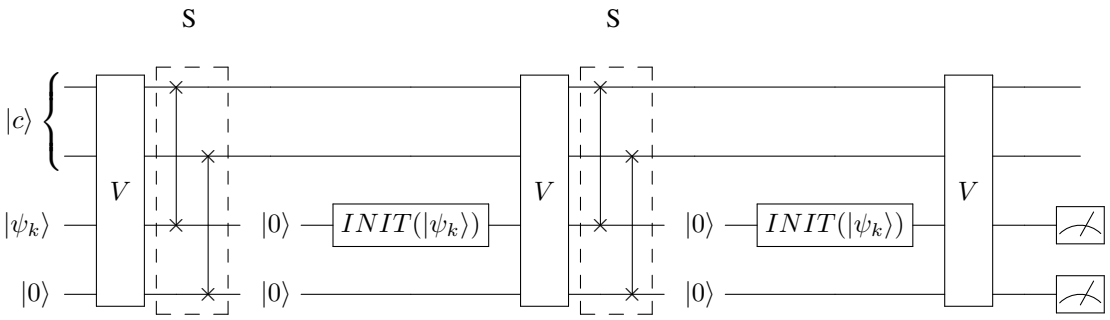

FIGURE 21: Three iterations of the optimized circuit simulating the D-CTC interaction. Reset operators ($|0\rangle$) let us not "waste" qubits and re-use them in the next iteration. $INIT(|\psi_k\rangle)$ gate maps the state $|0\rangle$ into $|\psi_k\rangle$. For the sake of readability, the figure represents the case in which $n = 2$, and the generalization is straightforward.

[17] L. Bacciottini, "Google drive repository." https://drive.google.com/file/d/1q9crwuFjhRLs0RAQ801SUbFQnCObJqlG/view. Last updated: 29 Nov 2021.
[18] K. M. R. Audenaert, J. Calsamiglia, R. Muñoz Tapia, E. Bagan, L. Masanes, A. Acin, and F. Verstraete, "Discriminating states: The quantum chernoff bound," Phys. Rev. Lett., vol. 98, p. 160501, Apr 2007.
[19] C. H. Bennett and S. J. Wiesner, "Communication via one- and two-particle operators on einstein-podolsky-rosen states," Phys. Rev. Lett., vol. 69, pp. 2881–2884, Nov 1992.
[20] H. Fan, K. Matsumoto, X.-B. Wang, and M. Wadati, "Quantum cloning machines for equatorial qubits," Physical Review A, vol. 65, Dec 2001.
[21] R. Blume-Kohout, S. Croke, and M. Zwolak, "Ideal state discrimination with an o(1)-qubit quantum computer," 2012.
[22] C. W. Helstrom, "Quantum detection and estimation theory," Journal of Statistical Physics, vol. 1, pp. 231–252, Jun 1969.